# A Gd-doped ceria/TiOx nanocomposite as the active layer in a three terminal electrochemical resistivity switch

Daniel Freidzon<sup>1</sup>, Ellen J. Wachtel<sup>1</sup>, Hagai Cohen<sup>2</sup>, Lothar Houben<sup>2</sup>, Anna Kossoy<sup>2</sup>, Olga Brontvein<sup>2</sup>, Maxim Varenik<sup>1</sup>, Anatoly I. Frenkel<sup>3,4</sup>, David Ehre<sup>1</sup> and Igor Lubomirsky<sup>1</sup>

<sup>4</sup>Division of Chemistry, Brookhaven National Laboratory, Upton, NY 11973, USA

Keywords: ion migration; reversible resistivity switching, composite, Gd-doped ceria

#### **ABSTRACT** (231 words)

Coupling between an electrochemical reaction and a functional material property has been termed electrochemo-X, or EC-X, where X can refer to mechanical, optical, magnetic or thermal properties. Recently, our group has demonstrated a two-terminal electro-chemo-mechanical (ECM) membrane actuator operating under ambient conditions and containing a Ce<sub>0.8</sub>Gd<sub>0.2</sub>O<sub>1.9</sub> solid electrolyte layer sandwiched between two Ce<sub>0.8</sub>Gd<sub>0.2</sub>O<sub>1.9</sub>/Ti oxide nanocomposite thin films. Reducing one nanocomposite film while oxidizing the other was observed to produce reversible volume change thereby driving membrane actuator operation. Here, we use the same electrolyte and nanocomposite layers to further explore the EC-X effect: we demonstrate proofof- principle for a functioning, three-terminal, thin film-based EC-electrical switching device operating at room temperature. We find that application of  $\pm 6V$  bias to the gate terminal for two hours under ambient conditions changes nanocomposite conductivity by at least 40%. When the bias is negative, the material remains in a more highly conductive state for approximately 24 hours. Impedance spectroscopy and cyclic voltammetry reveal oxygen ion migration taking place during device operation. Analyzing X-ray photoelectron spectroscopy data, we learn that, in the absence of negative gate bias, thermal oxidation of Ce<sup>+3</sup> -> Ce<sup>+4</sup> is similarly effective in leading to increased nanocomposite conductivity, while reduction produces the opposite effect. With the expectation that the response time can be significantly shortened, the proposed device may be suitable for future applications such as sensors, neuromorphic computing or spintronics.

<sup>&</sup>lt;sup>1</sup>Department of Molecular Chemistry and Materials Science Weizmann Institute of Science, Rehovot 7610001, Israel

<sup>&</sup>lt;sup>2</sup> Department of Chemical Research Support, Weizmann Institute of Science, Rehovot 7610001, Israel

<sup>&</sup>lt;sup>3</sup>Department of Materials Science and Chemical Engineering, Stony Brook University, Stony Brook, NY 11794, USA

#### 1 Introduction

Understanding and controlling mass transfer in solids under large chemical potential gradients is essential for practical application of materials in which a small change in stoichiometry may cause a significant change in material properties. In ion-conducting solids, an electric field (E-field) produces ion migration. If such a solid tolerates change in stoichiometry, those changes can be driven by an electrochemical reaction. Of particular interest is a material where a change in stoichiometry can modulate other properties. In many cases, such coupling has an adverse effect such as chemo-mechanical dimensional change in batteries or fuel cells[1-6] Coupling between an electrochemical reaction and a functional material property has been termed electrochemo-X, or EC-X, where X can refer to mechanical, optical, magnetic or thermal properties[1-3, 7-9]. An EC-X device generally contains a mixed ionic-electronic conductor, capable of changing stoichiometry under an E-field and serving as a reservoir (RV) for diffusing ions transported to/from the working body (WB). The WB is designed to display a large EC-X effect [7] produced by changes in the concentration of the diffusing ion. The RV and WB are separated by a solid electrolyte (SE) whose role is to support ion diffusion between the RV and the WB. As drawn in Figure 1, the upper metal contact, the RV and SE constitute an ion pump. Voltage application between the upper and lower electrical contacts produces a gradient of the chemical potential of diffusing ions at the SE-WB interface. This gradient leads to injection/extraction of ions from the WB, thereby promoting the EC-X effect. The design is similar to that of a battery, but it is meant to provide rapid changes in the composition of the WB rather than energy storage. Recently, an EC-mechanical (ECM) membrane actuator was demonstrated in our group[7, 10]. The ECM device was built as a multilayered structure comprising a ~1.5µm thick layer of 20mol% Gd doped CeO<sub>2</sub> (20GDC) placed between two nanocomposite WB's. Two versions of nanocrystalline composites suitable to serve as WBs have been developed[7, 11, 12] based on: VO<sub>x</sub>-GDC or TiO<sub>x</sub>-GDC composites. Application of DC or AC voltage between the metal contacts induces a flow of oxygen ions from one WB to the other. The oxidation of one WB along with reduction of the other produced a large mechanical response. The nanocrystalline structure of the composites allowed [7] rapid oxygen transport into/from the WBs providing a response time of less than one minute. Oxidation-reduction of the TiO<sub>x</sub>-GDC nano-composites was reported to be particularly rapid; however, exactly which element was undergoing the oxidation/reduction reaction could not be conclusively determined.

Here, we present proof-of-principle for a functioning, three-terminal (gate, source and drain), stacked thin film electrical switching device (**Figure 2**) based on reversible migration of oxygen ions operating at room temperature. We use the previously characterized Ti-GDC nanocomposite as both the working body and the ion reservoir and provide evidence that we can reversibly control conductivity *via* an electrochemical reaction. We have also determined, using X-ray photoelectron spectroscopy, that the oxidation-reduction reaction responsible for the observed effect is  $Ce^{3+}/Ce^{4+}$ .

#### 2 Material and Methods

### 2.1 Deposition conditions

The stacked lamellar structure was fabricated on a *c*-cut sapphire wafer, thickness ~430 μm. Ti metal electrodes were deposited from a Ti metal target (99.99% pure, Able targets, Ltd.) by DC magnetron sputtering under 5mTorr of Ar, 30sccm, 150W, for 3500 seconds at room temperature. The ceramic-containing layers were deposited by RF-magnetron sputtering (AJA international). The Ti-GDC nanocomposite layers (WB,RV) were deposited under reducing conditions: 20 mTorr Ar atmosphere, flow rate, 30sccm, with cosputtering from: (1) a Ti metal target (99.99% pure, 2" diameter, Able targets, Ltd.), DC-power of 150W and (2) a stoichiometric ceramic target (Ce<sub>0.8</sub>Gd<sub>0.2</sub>O<sub>1.9</sub>, 99.99% pure, 3" diameter, Able targets, Ltd.), RF power of 100W for 3000 seconds at room temperature. The 20GDC solid electrolyte (SE) was deposited from a stoichiometric ceramic target (Ce<sub>0.8</sub>Gd<sub>0.2</sub>O<sub>1.9</sub>, 99.99% pure, 3" diameter, Able targets, Ltd.), at 733K under 30 mTorr atmosphere of Ar:O<sub>2</sub>, 6:1 and 115W for 17500 seconds. A Ta oxide protective layer was deposited by reactive RF-magnetron sputtering from a Ta metal target (99.95% pure, 2" diameter, Kurt Lesker) at 298K under 10mTorr atmosphere of Ar:O<sub>2</sub>, 10:1 and 150W for 3600 seconds.

### 2.2 Multilamellar structure dimensions

Two separated bottom electrodes ("source" and "drain") were created by first depositing a 200nm thick Ti metal layer, followed by patterning with photolithography and etching, using a commercial, buffered oxide etch solution, thereby creating a 1mm wide channel. Both bottom electrodes were subsequently covered by the WB/SE/RV stack, where ~200nm thick Ti-GDC nanocomposite film was used for both the WB and the RV layers, and ~400nm thick 20GDC layer served as the SE. Upon deposition, the nanocomposite also fills the 1mm wide channel between the source and drain electrodes. The upper electrical contact, ~200nm Ti layer, was deposited on top of the RV, and using the same photolithography and etching process described above, the top "gate" electrode was defined. To avoid oxidation of the ion reservoir surface by atmospheric oxygen during device operation, a 500 nm thick Ta oxide layer was deposited by reactive magnetron sputtering and patterned by lift-off techniques (Figure 2).

#### 2.3 Electron microscopy of nanocomposite films

Samples for transmission electron microscopy, scanning electron microscopy (SEM) imaging and X-ray photoelectron spectroscopy (XPS) were prepared by depositing a ~470nm thick nanocomposite with the same sputtering parameters as those described above; however, deposition time was increased to 6000 seconds and the sapphire substrate was replaced by a p-Si(100), 0.01  $\Omega$ - cm,  $t_{Si}$  =280 $\mu$ m wafer (University Wafers). Si was chosen as it simplifies the process of sample preparation, and, according to X-ray diffraction profiles, does not alter the properties of the composite. A Helios 600 Focused Ion Beam (FIB) /SEM dual beam microscope (Thermo Fisher Scientific) was used to prepare a thin (~100nm) slice for subsequent TEM analysis. Energy dispersive X-ray spectroscopy (EDS) measurements were performed using a Titan Themis-Z (Thermo Fisher Scientific), an ultra-high resolution, double aberration-corrected, transmission electron microscope, equipped with a Super-X, large solid angle X-ray detector for EDS, operating at 200kV. High

resolution transmission electron microscopy (HRTEM) imaging and electron diffraction measurements were performed on a Talos F200X G2 microscope (Thermo Fisher Scientific), equipped with the Titan Themis-Z detector described above. High-resolution scanning transmission electron microscopy (HRSTEM) and 4D-STEM measurements were performed using a double aberration-corrected TFS Titan Themis-Z transmission electron microscope at 200 kV acceleration voltage. STEM images were recorded with a Fischione Model 3000 detector. Zero-loss filtered 4D-STEM datasets were obtained with a CEOS CEFID (CEOS GmbH, Heidelberg, Germany) energy filter, equipped with a DECTRIS ELA (DECTRIS AG, Baden, Switzerland) hybrid-pixel array detector for direct detection in counting mode. An electron probe with a convergence angle of 0.2 mrad and a real space probe diameter of about 6 nm was rastered across the sample for nanobeam diffraction experiments. A primary beam current of 4 pA and a frame time between 10 ms and 25 ms per raster position resulted in a total fluence of approximately 800 – 2000 e<sup>-</sup>/Å<sup>2</sup>. The SEM image of the Ti-GDC composite surface was obtained with a Zeiss Sigma 500 microscope.

#### 2.4 Electrical and structural characterization

Electrical characterization was performed using a B2912A Precision Source/Measure Unit, Keysight Technology Inc., internal ammeter resistance <200  $\Omega$ , and with impedance spectroscopy (IS) (ZG-4 with Alpha-A modular measurement system, Novocontrol Technologies GmbH and Co. KG) in the frequency range 1MHz to 1mHz. In order to characterize the electrical properties of the multi-lamellar sample and of the Ti-GDC nanocomposite, Ti electrodes were connected to copper wires using silver paint. Conductivity under ambient conditions of the 1mm wide nanocomposite filled channel, prior to or following application of either positive or negative bias ( $V_{gate}$ ) to the shorted source-drain electrodes, was measured for at least 3 cycles, and for 5 samples. X-ray diffraction (XRD) measurements were performed on a SmartLab (Rigaku, Japan) diffractometer equipped with a rotating Cu anode ( $K_{\alpha}$ , $\lambda$ = 1.540Å; a Ni filter in the diffracted beam removed Cu  $K_{\beta}$ ) operating at 45 kV and 200 mA and with a HyPix-3000 two-dimensional detector. For Bragg-Brentano geometry measurements, the incident X-ray beam was shaped by a 2.5° Soller slit; a second 2.5° Soller slit was placed after the sample. Variable divergence slits were used. The widths of the scattering and receiving slits were both 5 mm. Step size was 0.025°. Data acquisition was conducted with the detector in the 1D mode and lasted approx. 1 hour. A 3° sample offset was used in order to avoid strong diffraction from the single crystalline substrate.

# 2.5 X-ray photoelectron spectroscopy (XPS)

XPS measurements were performed on a Kratos Axis Ultra-DLD spectrometer, using a monochromatic Al K $_{\Box}$  source at two power levels, 15 and 75 W. In view of the finite stability of the effects of annealing the Ti-GDC nanocomposite film, an attempt was made to have relatively short pumping periods following sample insertion into the UHV chamber. Data presented here are for samples undergoing 4 hours of pumping prior to the beginning of measurements. For films deposited on sapphire, charge neutralization with an electron flood gun (eFG) was essential in order to eliminate unavoidable positive charging under XPS scans. This was found to affect the photoelectron spectra by reducing  $Ce^{4+}$  to  $Ce^{3+}$ . On the other hand, films grown on p-doped Si wafers

could be measured without using the eFG and thus provide a more reliable evaluation of the Ce oxidation states. The extent of charging still present was evaluated by comparing scans under different source conditions and, in addition, under application of the eFG. Effects of X-irradiation were inspected as well, revealing minor beam-induced modifications, which were studied and taken into account in the analysis.

#### 3 Results and discussion

#### 3.1 Demonstration of device functionality

To demonstrate device functionality under ambient conditions, 6V bias was applied for 2 hours between the gate and the shorted source-drain Ti electrodes (**Figure 2B**) to induce oxygen ion migration from the gate electrode reservoir into the channel. A period of two hours was chosen to minimize irreversible degradation in device performance which was found to occur at longer times (see Supplementary materials, Figure S1). The bias voltage and shorting connection were then removed and the change in the resistance of the channel examined. Resistance of the 1mm channel between the source and drain was monitored by acquiring an I-V voltammogram at scan rate 104 mV/s (**Figure 3A**). Channel resistance was calculated by linear regression on each I-V curve for  $|V| \le 1$  volt. Application of negative voltage on the gate along with positive voltage on the shorted source - drain electrodes clearly lowers channel resistance, while the reverse bias increases channel resistance. Both the low and the high resistance states are characterized by moderate hysteresis which likely result from capacitive current [13]. A factor of  $4.1\pm0.9$  was calculated to be the average change in resistivity, with statistical uncertainty based on at least 3 cycles, 5 samples. The retention time, which is the time required for the channel to return from a low to a high resistance state, was also monitored at the same scan rate and estimated to be approx. twenty-four hours (**Figure 4**):the average resistivity was found to increase linearly with time at rate  $90 \text{ k}\Omega \cdot \text{m} \cdot \text{s}^{-1}$ .

### 3.2 Cyclic voltammetry of the stacked lamellar structure

Cyclic voltammetry of the stacked lamellar structure with voltage applied between the gate and the shorted source / drain electrodes (see Figure 2B) was measured in air (Figure 5A-C) at room temperature and at 363K to investigate charge transfer between the top and bottom nanocomposites. We note that the maximum voltage in this experiment corresponds to an electric field < 20 kV/cm, which is too weak to induce field-accelerated ion mobility[14]. All three panels of Figure 5 display an increase in conductivity with applied voltage. This is a characteristic of memristors. However, the pinched hysteresis loop of a memristor (*i.e.*, intersection of negative-going and positive-going curves of a cycle) should occur at V=0[15], while in Figure 5, that is not the case. Two explanations may be found for the observed shift of the intersection point:(i) the existence of a capacitor in parallel with the memristor element[16, 17]and/or (ii) the existence of an internal electromotive force that may arise due to a gradient in the concentration of oxygen vacancies[16, 18]. Enlargement of the upper, positive voltage quadrant in panel B reveals current maxima (marked with black dots), indicating a diffusion-limited electrochemical reaction [19]. Given that such maxima are observed only when positive voltage is applied and that the cyclic voltammograms measured at different scan rates do not obey the Randles–Sevcik relation [19] (see Supplementary , Figure S2), suggests that the electrochemical reaction

may not be completely reversible and/or it is not limited by diffusion[19]. We attribute the significantly higher current observed in the lower negative voltage quadrant to the larger total surface area of the two bottom electrodes, as compared to the gate electrode.

### 3.3 Thermal oxidation and microstructure of an uncovered Ti-GDC nanocomposite working body (WB)

To provide supporting evidence that oxidation of the WB - thermally as well as electrically - is responsible for an increase in conductivity (**Figure 3A, B**), a second device was designed and prepared on a sapphire substrate, consisting of the Ti metal source and drain electrodes (thickness 200nm), an exposed Ti/GDC nanocomposite WB layer (470nm) and a nanocomposite-filled, 1mm wide channel between the Ti source and drain electrodes. Deposition under reducing conditions was performed with the same parameters as those used for the multilayer device. Samples were then heated under either oxidative (23 hours, 633K, air) or non-oxidative, *i.e.*, reducing (23 hours, 633K, N<sub>2</sub> atmosphere) conditions. Channel conductivity was monitored at room temperature both before and after thermal treatment (**Figure 6A**). It is evident that thermal treatment under oxidative conditions significantly reduces nanocomposite resistance. In addition, conductivity spontaneously drops with time, eventually returning to its initial value. Thermal treatment of the WB in inert atmosphere revealed no change in conductivity (**Figure 6B**), which remained very low.

XRD patterns of a 470nm thick *Ti-GDC* nanocomposite film deposited directly on a sapphire substrate were measured both before and after 23 hours of thermal treatment at 633K in air. (Error! Reference source not found.). The XRD pattern of an as-deposited sample features broad peaks typical of nanocrystalline material, similar to the XRD pattern reported for sol-gel *Ti-Ce-O*<sub>2</sub> thin films[20, 21]; the minimum crystal size was estimated from the peak width. The patterns remain essentially unchanged upon annealing.

TEM and STEM electron microscopy data of an as-deposited 470nm thick Ti-GDC film on silicon are presented in **Figure 7.** The SEM micrograph of the surface of the Ti-GDC composite (**Figure 7A**) reveals densely packed grains, with an average transverse grain size of ~ 37±2nm determined by the lineal intercept method. Whereas the XRD nanocrystallite size determined with the Scherrer formula from the first diffraction peak points to a minimum crystal dimension below 2 nm, the larger transverse grain size from SEM reflects a tendency of such grains to agglomerate. The STEM dark-field image of a cross-sectional TEM sample in **Figure 7B** shows a columnar morphology with columnar grains extending from the substrate to the surface. The column diameters match the average length scale of the features in the SEM image. EDS elemental mapping provides evidence for compositional homogeneity across the column boundaries (**Figure S4**). The column boundaries are, therefore, considered to be regions of lower material density.

Scanning nanobeam electron diffraction experiments, a variant of 4D STEM [22], gave further evidence of the nanocrystalline structure of the composite. For these experiments, a fine electron beam moved across a selected region, and a full diffraction pattern was recorded for each scan position. A probe size of about 6 nm combined with a scan step size of 1.7 nm provided finely detailed diffraction information on a scale smaller than the column size of the composite. **Figure 7C** displays a virtual dark-field intensity image obtained from an angular detection range selecting the first sharp electron diffraction peak. The map shows intensity related

to coherent scattering contrast that fluctuates on a lateral scale of a few nm. Summing the diffraction patterns obtained from the large region of interest (ROI) across the scanning raster (**Figure 7D**), resulted in broad scattering rings consistent with the results obtained from XRD. The inspection of single diffraction patterns from within the scanning raster (**Figure 7E**) reveals that the first diffraction peak consists of Bragg pairs of diffracted intensity, providing evidence of the existence of small crystalline domains. Random noise in the counting statistics for a single diffraction pattern could be ruled out as a source for the spots on the diffraction ring: hundreds of successive 20 ms frames in time series (not shown here) of electron diffraction taken from a single spot on the sample showed a high degree of temporal correlation between successive frames that is not consistent with noise dominating the ring intensity.

## 3.4 Impedance spectroscopy

To gain further insight into the mechanism underlying the operation of the proposed resistivity switch, impedance spectroscopy measurements were made between the Ti metal source and drain electrodes under ambient conditions, excitation voltage 0.2V AC, frequency range 1MHz to 1mHz, with or without application of 3.5 volts DC. Nyquist plots in the complex plane (**Figure 8**) display a single arc, interpreted as a superposition of the grain core and grain boundary impedance of GDC. Both arcs may be fit to depressed semi-circles -Im(Z)= $y_0$ +[ $R_0$ -( $R_0$ -( $R_0$ -( $R_0$ -( $R_0$ - $R_0$ -) $R_0$ -1 in parameters are tabulated in Error! Reference source not found. DC voltage application reduces the impedance of the WB composite in the 1mm channel, indicative of ion blocking interfaces [23]. Although ref. [23]reports that only grain boundary, and not grain core, impedance is affected, as we note above, at and near room temperature, GDC grain core and grain boundary impedance cannot be separated.

Impedance spectroscopy of the multilamellar stack (see Figure 2) provides an independent method (aside from cyclic voltammetry) for characterizing electrochemically promoted conductivity as well as its dependence on temperature (Figure 9A-C). Impedance was measured between the gate and the shorted source / drain electrodes with 0.05V AC excitation voltage, frequency range 1MHz to 1mHz at: A) room temperature; B) 323K; and C)363K. All panels display a high frequency arc corresponding to the superimposed grain core and grain boundary conductivity. Although the total conductivity does increase with temperature, the increase in temperature is apparently insufficient to separate the arc related to the grain core from that the grain boundary. The low frequency feature corresponds to the polarization of the nanocomposite/electrode interface, due to the ion blocking properties of the Ti electrodes. As described above, the high frequency arc was fit to a depressed semi-circle using a parallel resistor-capacitor equivalent scheme:  $Im(Z)=y_0+[R_0-(Re(Z)-X_0)^2]^n$ . The fitting parameters are tabulated in **Table S2**. An Arrhenius-type graph, using the resistance (R<sub>o</sub>) found from the fitting of the high-frequency arc, permitted determination of the activation energy for total conductivity between room temperature and 363K to be ~1.01eV. This value is commonly found for bulk lanthanide doped ceria at intermediate temperatures, i.e.,~ 800K, where oxygen ion conductivity dominates over electron conductivity [24]. Focusing on the low frequency feature, a Bode-type, log-log plot of -Im(Z) vs frequency (f) (Figure S5) allows fitting to the expression:  $-\text{Im}(Z) = (i2\pi fC)^{-n}$  where C is capacitance. This is readily used to identify the presence of a constant phase element (CPE) at low frequency [25]. When n = 1, the element is said to behave as pure capacitance; when n=0.5, a Warburg element is present; and when 0 < n < 1, we recognize diffusion-controlled capacitance. Fitting parameters and the frequency region fit are tabulated in **Table S3**, revealing that indeed at temperatures weakly above ambient, the multilamellar device displays ion diffusion which controls its low frequency behavior.

## 3.5 X-ray photoelectron spectroscopy (XPS) of the Ti-GDC nanocomposite

As shown in **Figure 10**, pronounced spectral differences are found between the 'as deposited' and 'annealed' nanocomposite films. These differences are primarily detected in the Ce-related spectral windows: (1) *Ce 3d*; (2) *Ce 4d*; and (3) the valence band regime, where the *Ce 4f* orbitals correspond to the lowest binding energy peak (~ 2 eV). Remarkably, the spectra of Gd, Ti, O (and C, attributed to adsorbed organic molecules) show only minor changes due to annealing for 23hr at 633K: a minimal increase in oxygen content and almost no change in the Ti oxidation state. The small yet finite shifts seen in **Figure 10** express finite surface charging that is absent from the earlier (fast, hence noisy; data not shown) scans. In essence, the observed differences suggest that the main effect of annealing was to transform Ce<sup>3+</sup> to Ce<sup>4+</sup>[26, 27]. This oxidation is manifested by pronounced amplitude changes at the Ce shake-satellites; shake-signal assignments are indicated in the Figure. Also readily observable is the difference in amplitude and position of the main Ce 4d<sub>5/2</sub> and Ce 3d<sub>5/2</sub> peaks, indicated in the Figure by arrows. Finally, the Ce 4f peak (at ~2 eV, closest to the Fermi level) is clearly emptied by the annealing process, as expected.

Notably, a mixture of Ce <sup>3+</sup> and Ce<sup>4+</sup> is found in both cases, before and after annealing, however with markedly different relative amplitudes. Whether such coexistence of Ce-oxidation states is essential or not for effective oxygen diffusion is yet unclear. However, an independent indication for the lability of oxygen atoms is provided by an 'artifact-like' effect, where small changes in the relative amounts of Ce<sup>3+</sup> and Ce<sup>4+</sup> are observed upon long exposure to the X-irradiation. **Figure 10F** and **Figure S6** compare spectra recorded for repeated measurements at a fixed sample position. **Figure 10F** exhibits a slight decrease with time in the amount of Ce<sup>4+</sup> and, in turn, a corresponding increase in Ce<sup>3+</sup> signals. The corresponding Ti 2p and O 1s spectra do not show any apparent changes except for minor surface charging that occurred during that period of time. Consequently, the beam-induced artifact reveals that, given a supply of energy by the X-ray photons, oxygen atoms in the vicinity of Ce<sup>4+</sup> sites are the 'first' to slightly move and rearrange their chemical bonds. The result also supports our claim for oxygen diffusion-related functionality.

#### 4 Conclusion

In the current study, we present proof-of-principle for a three-terminal device, based on a Ti-GDC nanocomposite working body, which exhibits resistive switching behavior driven by an electrochemical reaction. Cyclic voltammetry reveals both memristive-type behavior and electrochemical coupling. Combined with elevated temperature (363K) impedance spectroscopy of the lamellar stack, these data provide evidence that reversible oxygen ion migration under low electric fields (<20 kV/cm) is responsible for the observed resistive switching. This is in contrast to commonly observed memristive behavior known to occur in Gd-

doped ceria under high electric field (>>100 kV/cm) and has been associated with the formation of conductive oxygen vacancy filaments due to field-accelerated migration [15, 28, 29].

A possible explanation for how oxidation increases the Ti-GDC nanocomposite conductivity may be found in a suitable variant of the space charge model of [30, 31]. We note that nanocrystallinity introduces such a high density of interfaces/grain boundaries that total conductivity may become interfacially controlled. Grain boundaries in doped ceria lack long range order and are relatively rich in oxygen vacancies and  $Ce^{3+}$ , which, along with the space charge zone which forms for charge neutrality, produce a blocking effect for ion conduction. Oxidation of  $Ce^{3+} -> Ce^{4+}$  leads to a lowering of total real charge, causing the spatial extent of the space charge zone to shrink as well. Finally, this succeeds in lowering the potential barrier for ion diffusion across the grain boundary, which increases the overall conductivity. Reduction of the Ti-GDC nanocomposite produces the opposite effect.

# 5 Acknowledgements

I.L. acknowledges the BSF program grant 2018717 for the studies of the ECM working bodies. A.I.F acknowledges the support by the NSF Grant number DMR-1911592 for his contribution to the studies of the ECM working bodies. These grants are the two parts of the NSF-BSF grant awarded to A.I.F. and I.L., respectively.

## 6 Figures and tables

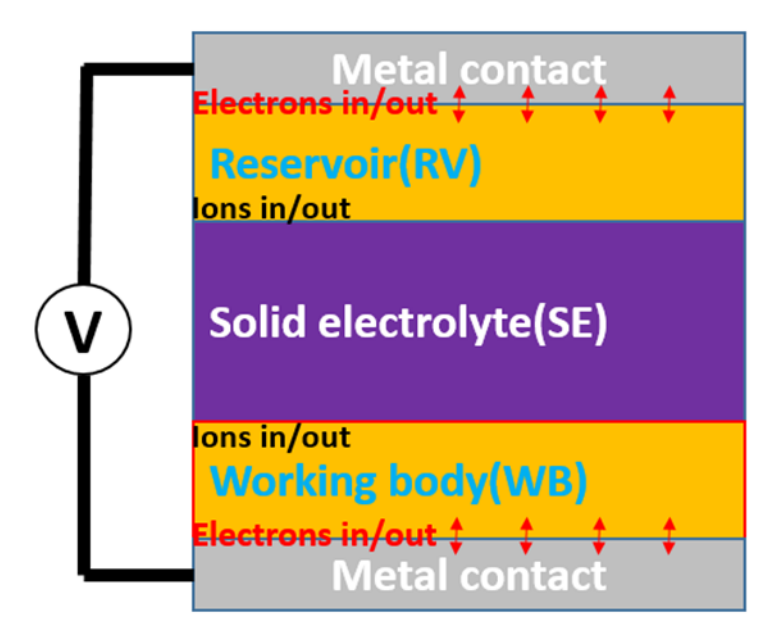


**Figure 1.** Scheme of a typical device, the functioning of which depends on electrochemically driven changes in stoichiometry.

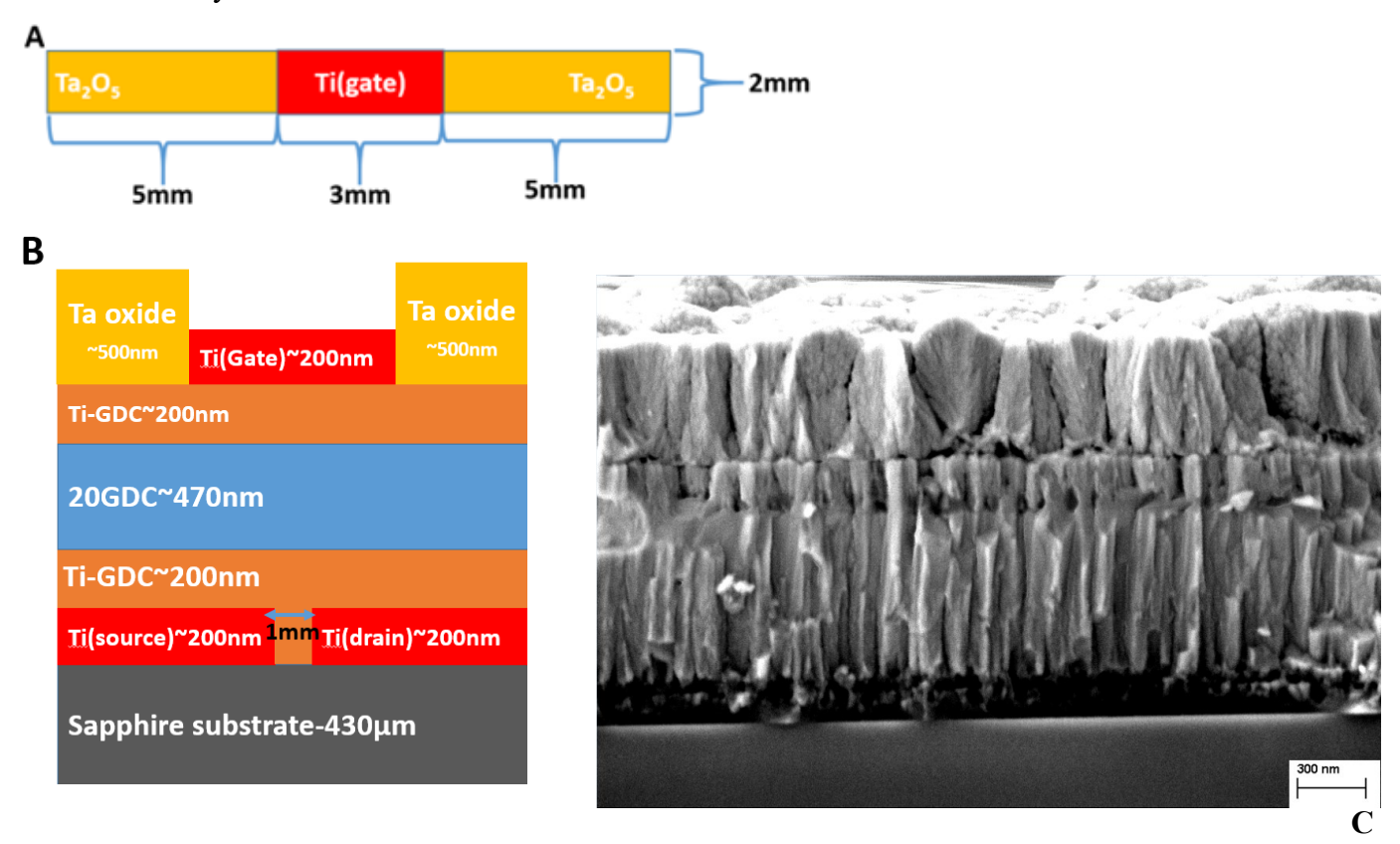


**Figure 2.A)** Top view and **B)** cross-section view of the stacked lamellar structure with Ti-GDC composite thin films separated by the solid 20GDC electrolyte. The 1mm wide channel is created as follows. First, a uniform Ti layer is deposited on the sapphire substrate and the 1 mm gap between the source and drain is defined using photolithography and subsequent etching. The Ti-GDC working body is then deposited and also fills the 1 mm wide channel between the source and drain. The diagram is not to scale. **C)** Cross-section SEM micrograph where the section has been cut at a location which is not covered by the Ti gate electrode. The bottom Ti-GDC/20GDC interface is not well defined when compared to the corresponding top interface. This difference may be attributed to the exposure of the bottom Ti-GDC film to high temperature during 20GDC deposition, while the top Ti-GDC film is not exposed to high temperature during the fabrication process.

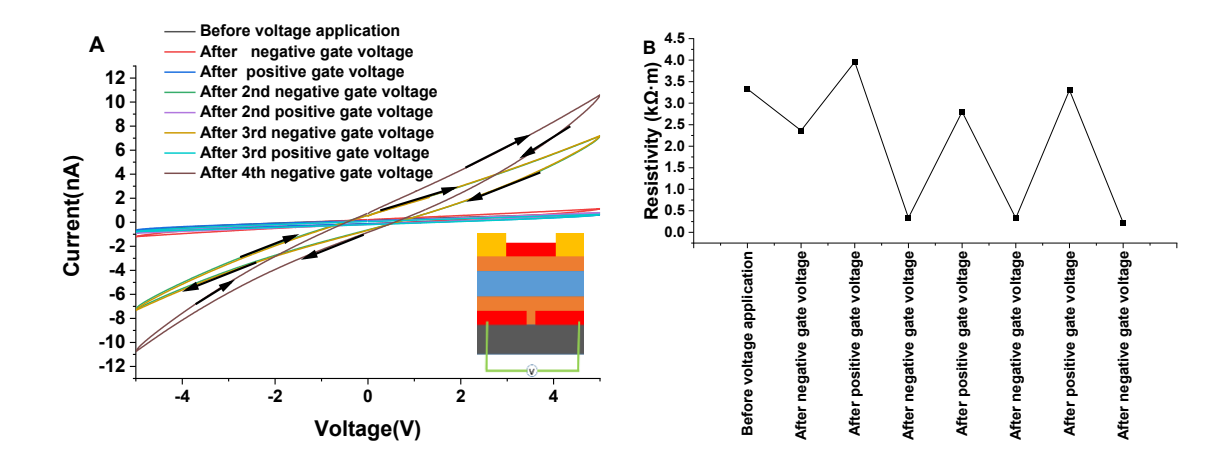
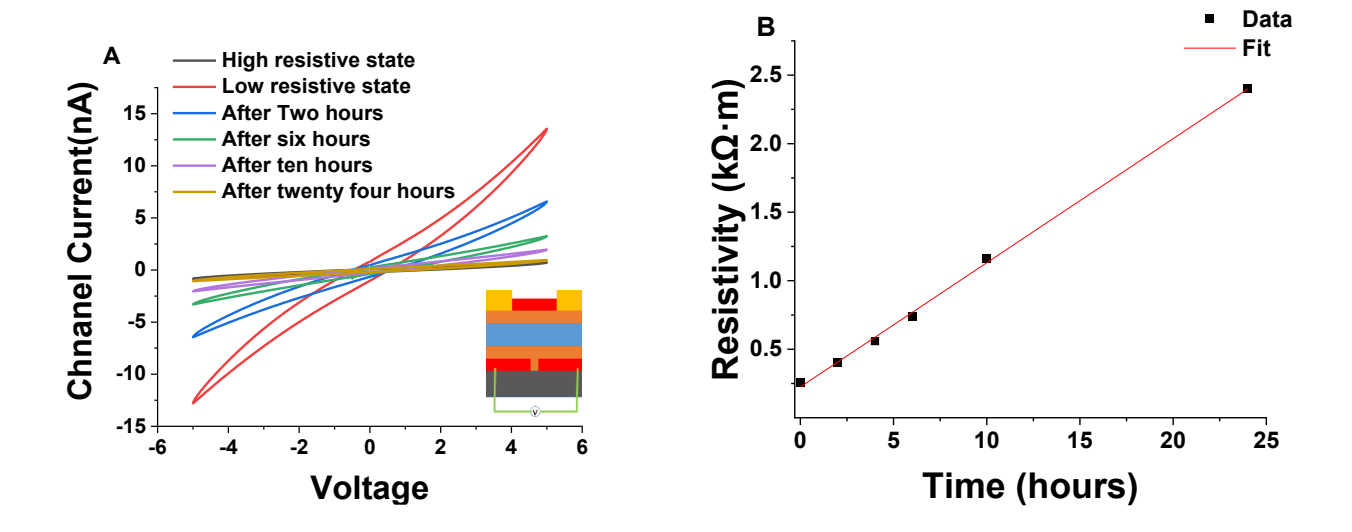
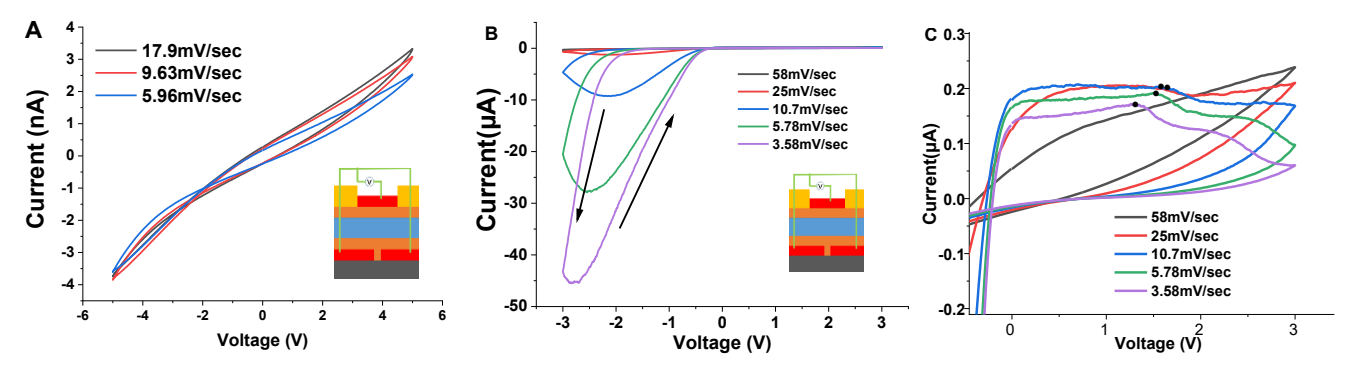


Figure 3. Demonstration of resistive switching of the multi-lamellar device (see Figure 2). First, 6V bias voltage was applied between the gate and the shorted source/drain electrodes for 7200 seconds. (N.B., positive gate voltage indicates that the gate serves as the positive electrode and the shorted source/drain, the negative electrode; negative gate voltage indicates the bias is reversed). Then, the bias voltage and the shorting connection between the source and drain were removed. (A). Cyclic voltammograms with scan rate 104 mV/s were measured between the source and drain electrodes. In the low resistance state, hysteresis is evident. The process was repeated for at least 3 cycles for each of 5 samples. (B) Channel resistance was calculated from the cyclic voltammograms by linear regression for  $|V| \le 1$  volt. The resistance was calculated to change by a factor of  $4.1\pm0.9$ . Statistical uncertainty is based on 3 cycles, 5 samples.



**Figure 4. (A).** Probing retention time using cyclic voltammetry reveals a decrease in conductivity with time of the composite-filled 1mm channel (between the source and drain electrodes) after achieving a low resistance state. The low resistance state is observed following application of negative voltage to the gate and positive voltage to the shorted source / drain electrodes. The retention time, i.e., the time required to pass from a low resistivity state to a high resistivity state under ambient conditions, is estimated to be ~24 hours. **(B).** Resistivity increases linearly with time during this period. The scan rate was 104 mV/s. Choice of scan rate was dictated by the relaxation time of the low resistivity state.



**Figure 5.** Cyclic voltammetry in air of the stacked lamellar structure with voltage applied between the gate and the shorted source / drain at: **A)** room temperature and **B)** at 363K. All three panels display an increase in conductivity with applied voltage. This is characteristic of memristance, as is also evidenced by a pinched hysteresis loop[32] (i.e., negative-going and positive-going curves of a cycle intersect). Although intersection should occur at V=0 to identify a memristor[15, 17, 33, 34] explanations for non- intersection at V=O have been proposed [16, 18]. **C)** Enlargement of the upper positive voltage quadrant in Figure B), which displays current maxima (marked with black dots), indicating the presence of a diffusion-limited electrochemical reaction[19]. We suggest that the larger total surface area of the two bottom electrodes, as compared to the gate electrode, is responsible for the significantly higher current observed in the lower negative voltage quadrant. The low scan rate was chosen to facilitate observation of diffusion-limited electrochemical reaction current peaks.

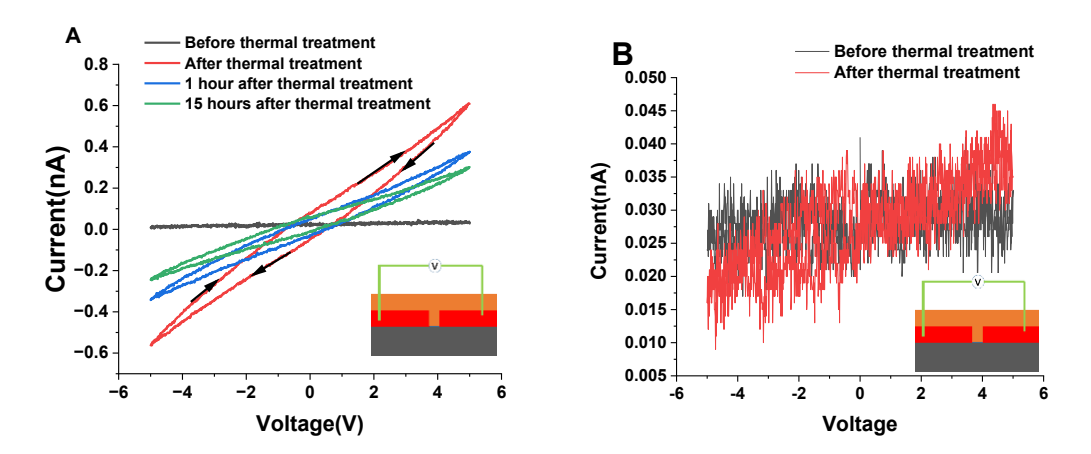


**Figure 6.** Cyclic voltammograms obtained for a sample consisting only of the 200nm thick WB nanocomposite layer, and the Ti metal source and drain electrodes separated by the nanocomposite filled 1mm wide channel, measured before and after thermal treatment at 633K for 23 hours: A) in air and B) under high vacuum. The scan rate in both panels was 104mV/s. We note that there is current at zero voltage in both panels. This is likely due to the presence of charge in the WB filled channel which then discharges when the sample is connected to the voltage source. This charge, either ions or electrons, is suggested to be trapped in the WB as a result of the low conductivity of the sample.

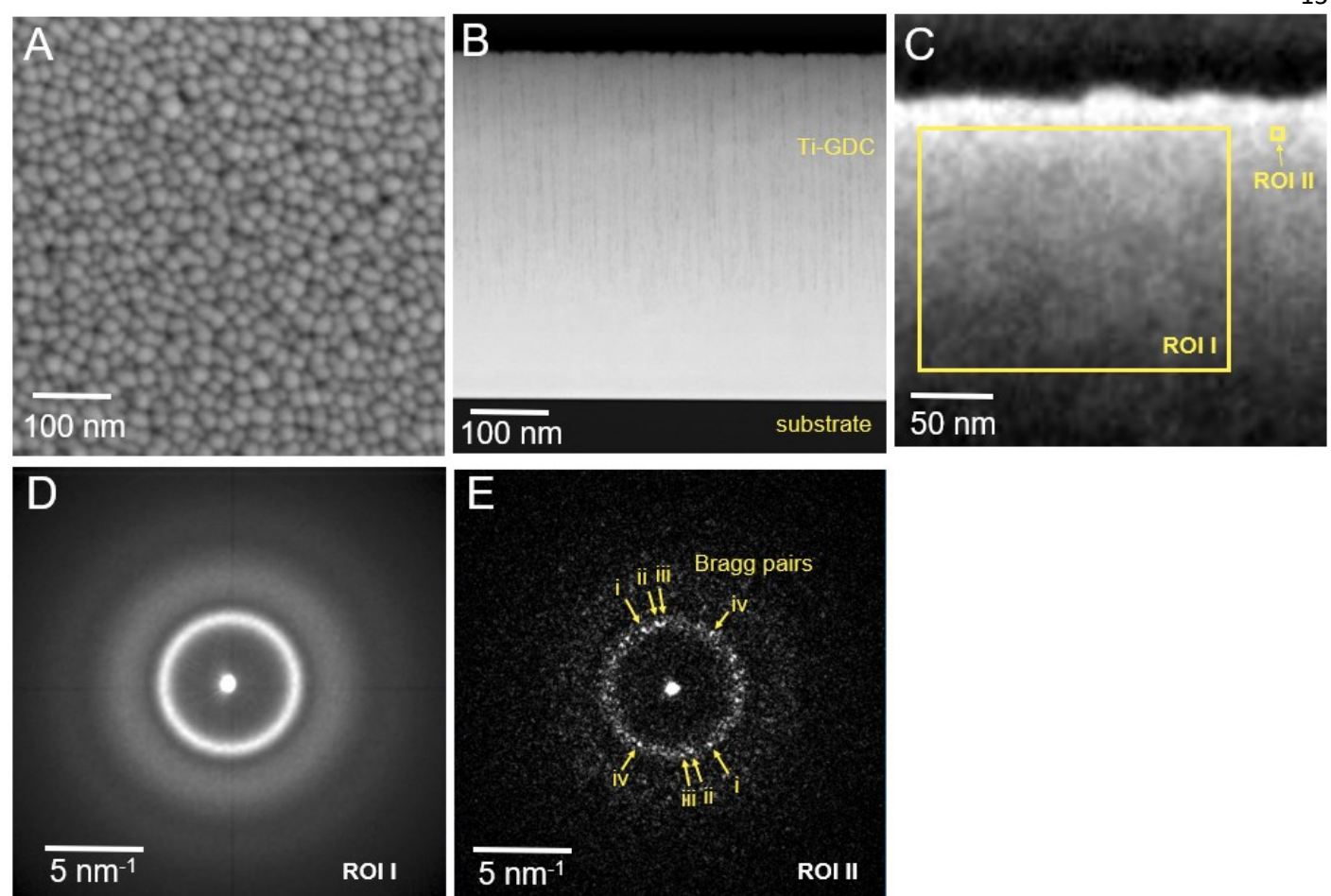
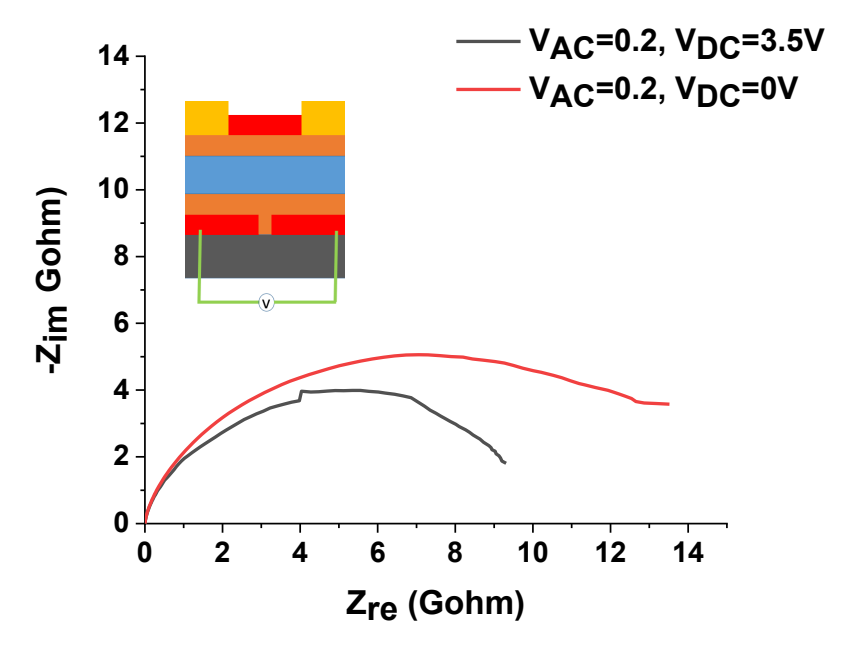
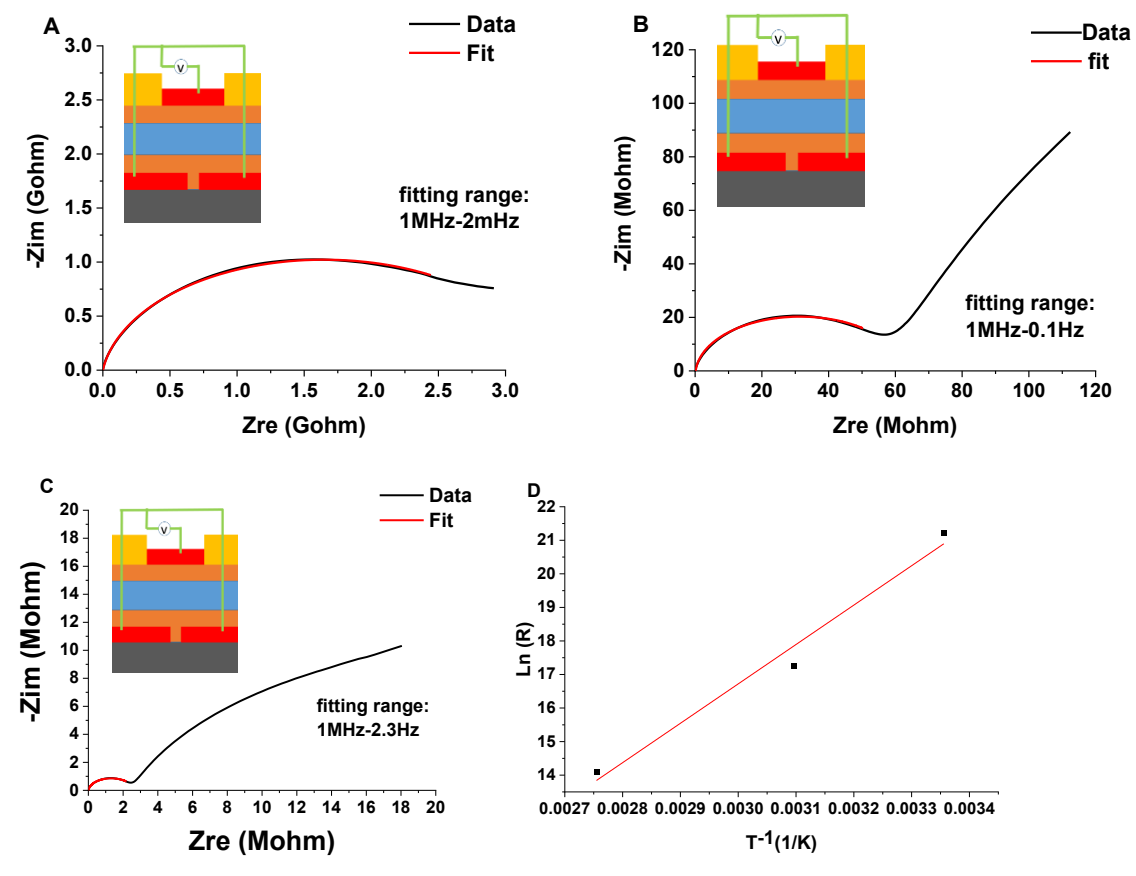


Figure 7. Electron microscope images of the 470nm thick Ti-GDC nanocomposite deposited on the Si wafer substrate. A) SEM micrograph of the surface of the Ti-GDC composite. The average transverse grain size is  $37\pm2$ nm. B) Annular dark-field STEM image of a cross-sectional sample of the composite deposited on Si and coated with carbon to minimize charging. The image shows a columnar morphology with column diameter consistent with the average grain size observed in SEM. Mapping of the homogeneous elemental distribution in the Ti-GDC composite as well as elemental quantification are provided in Supplementary materials (Figure S4; Table S1). C) 4D STEM image. Virtual annular dark-field obtained from the first diffraction ring located at a lattice spacing of approx.. 3 Å. The speckled, cauliflower-like contrast is related to diffraction from coherent domains with size a few nm. Scan raster: 153 x 153 pixels², pixel size: 1.7 x 1.7 nm². D) Average diffraction pattern obtained by summing all patterns obtained in the region of interest I marked in C). Diffuse diffraction rings match those observed in XRD patterns. E) Superposition of diffraction patterns obtained from the 3.4 x 3.4 nm² region of interest (ROI II in C)). The first diffraction ring is made up of diffraction spots. Bragg pairs associated with small crystalline domains on the nanometer scale can be readily identified. Four of these pairs are marked.



**Figure 8.** Impedance measurement between the Ti metal source and drain electrodes under ambient conditions, excitation voltage 0.2V AC, frequency range 1MHz to 1mHz, with or without application of 3.5 volts DC. Both Nyquist plots display a single arc, interpreted as a superposition of the grain core and grain boundary impedance of GDC. Both arcs may be fit to depressed semi-circles -Im(Z)= $y_0$ +[ $R_0$ -( $R_0$ -( $R_0$ -( $R_0$ - $R_0$ -) $R_0$ -), where ( $R_0$ -), where ( $R_0$ -), where ( $R_0$ -) define the center of the circle. Fit parameters are tabulated in Table 1. DC voltage application reduces the impedance of the WB composite in the 1mm channel, indicative of blocking interfaces [23]. Although [23] report that only grain boundary, and not grain core, impedance is affected, we note that under ambient conditions, GDC grain core and grain boundary impedance cannot be separated.



**Figure 9.** Impedance spectroscopy of the multilamellar stack (see Error! Reference source not found.) measured between the gate and the shorted\_source / drain\_with 0.05V AC excitation voltage at: **A)** room temperature; **B)** 323K; and **C)**363K. All figures display a high frequency arc corresponding to the superimposed grain core and grain boundary conductivity. The low frequency feature corresponds to the polarization of the composite/electrode interface, due to the ion blocking properties of the Ti electrodes. The high frequency arc was fitted to a depressed semi-circle using (as described above)  $-\text{Im}(Z)=y_0+[R_0-(Re(Z)-X_0)^2]^n$ . The fitting parameters are tabulated in Table S1. **D)** Arrhenius-type graph using the resistance ( $R_0$ ) found from the fitting of the high-frequency arc. The calculated activation energy is 1.01eV. The imaginary component of the impedance measured at 323K and 363K was also replotted as a log-log Bode-type plot (see **Figure S5**).

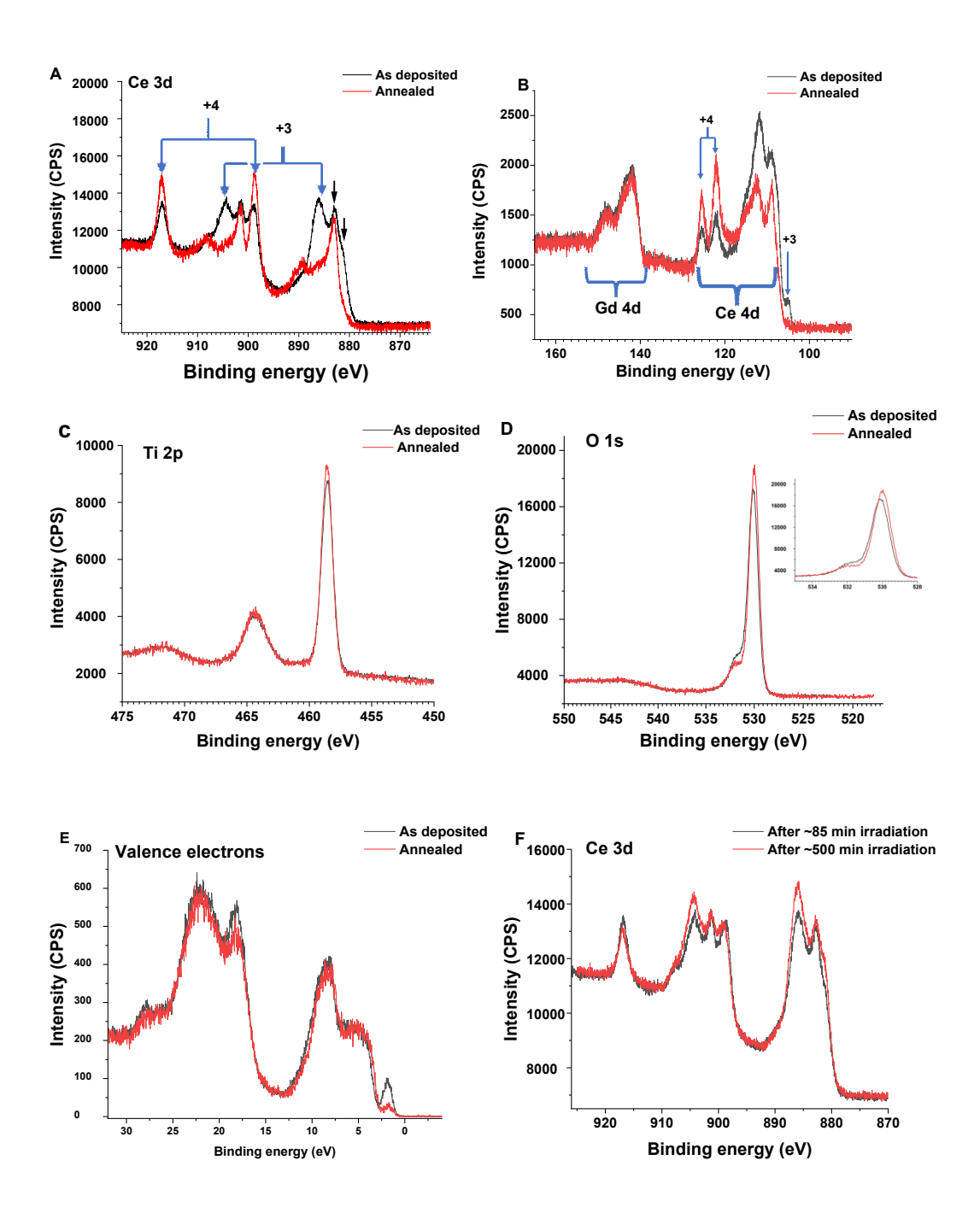


**Figure 10.** XPS spectra of the as-deposited (black) and annealed in air (red) Ti-GDC nanocomposite films, deposited on p-Si wafers: (**A**) Ce 3d; shake-satellites of the Ce lines are indicated with blue arrows, for convenient identification of the  $3^+$  and  $4^+$  Ce oxidation states; ; arrows ( $\downarrow$ ) marking the **main** Ce  $d_{5/2}$  peak of the  $3^+$  and  $4^+$  states are added as well; (**B**) Ce 4d and Gd 4d; (**C**) Ti 2p; (**D**) O 1s; (E) valence electron regime, including the Ce 4f states. Beam induced effects are demonstrated in (F) showing the Ce 3d spectrum of an as-deposited layer, recorded following two different exposure times to the X-ray beam. Note the obvious differences in Ce spectra, (panels A, B and E,) while the Ti, Gd and O spectra, (panels B, C and D), exhibit only minor changes, if any. Additional time dependent XPS spectra are shown in the Supplementary materials section.

Table 1.Depressed semi-circle parameters for Nyquist plots (**Figure 8**) in the complex impedance plane under ambient conditions. (y<sub>0</sub>, x<sub>0</sub>) are the coordinates of the center of the depressed semi-circle; R<sub>0</sub> is the radius of the semi-circle; n = 0.5 defines a perfect circle:  $\alpha = 1 - \frac{2}{\pi} tan^{-1}(\frac{y_0}{x_0})$ .  $\alpha = 1$  identifies homogeneous relaxation.

V <sub>DC</sub>	yo	Xo	$R_0$	n	
<b>(V)</b>	(Gohm)	(Gohm)	(Gohm)		
0	0.434(±9.4%)	7.02(±0.05%)	7.65(±0.07%)	0.492(±0.04%)	~1
3.5	-0.316(±11%)	5.01(±0.09%)	4.98(±0.06%)	0.495(±0.04%)	~1

#### References

- [1] X.J. Wang, F.F. Fan, J.W. Wang, H.R. Wang, S.Y. Tao, A. Yang, Y. Liu, H.B. Chew, S.X. Mao, T. Zhu, S.M. Xia, *Nat. Comm.* **6** (2015)
- [2] J.L.M. Rupp, E. Fabbri, D. Marrocchelli, J.W. Han, D. Chen, E. Traversa, H.L. Tuller, B. Yildiz, *Adv. Func. Mater.* **24** (2014) (11) 1562
- [3] J.G. Swallow, J.J. Kim, J.M. Maloney, D. Chen, J.F. Smith, S.R. Bishop, H.L. Tuller, K.J. Van Vliet, *Nat. Mater.* **16** (2017) (7) 749
- [4] S.R. Bishop, N.H. Perry, *Electro-Chemo-Mechanics of Solids* (2017) 1
- [5] C.S. Kim, S.R. Bishop, N.H. Perry, H.L. Tuller, *J. Electroceram.* **38** (2017) (1) 74
- [6] Y.-L. Zhang, J.-C. Li, H. Zhou, Y.-Q. Liu, D.-D. Han, H.-B. Sun, *The Innovation* 2 (2021) (4)
- [7] E. Makagon, E. Wachtel, L. Houben, S.R. Cohen, Y.Y. Li, J.Y. Li, A.I. Frenkel, I. Lubomirsky, *Adv. Func. Mater.* **31** (2021) (3)
- [8] L. Ji, G.X. Zhang, Z.Q. Li, H.Y. Cao, S.P. Shen, *Nanoscale* **14** (2022) (37) 13651
- [9] D.S. Tsvetkov, V.V. Sereda, D.A. Malyshkin, I.L. Ivanov, A.Y. Zuev, J. Mat. Chem. A 10 (2022) (12) 6351
- [10] J. Li, Y. Li, P.K. Routh, E. Makagon, I. Lubomirsky, A.I. Frenkel, J. Synchrotron Rad. 28 (2021) (5) 1511
- [11] E. Makagon, J. Li, Y. Li, E. Wachtel, A.I. Frenkel, I. Lubomirsky, Sol. State Ionics 379 (2022) 115913
- [12] J. Li, P.K. Routh, Y. Li, A. Plonka, E. Makagon, I. Lubomirsky, A. Frenkel, J. Synchrotron Rad. 30 (2023) (4)
- [13] S. Zhu, G. Zhou, W. Yuan, S. Mao, F. Yang, G. Fu, B. Sun, Journal of colloid and interface science 560 (2020) 565
- [14] L. Onsager, The Journal of chemical physics 2 (1934) (9) 599
- [15] R. Schmitt, J. Spring, R. Korobko, J.L. Rupp, Acs Nano 11 (2017) (9) 8881
- [16] B. Sun, M. Xiao, G. Zhou, Z. Ren, Y. Zhou, Y. Wu, Materials Today Advances 6 (2020) 100056
- [17] I. Riess, J. Electroceram. 39 (2017) (1-4) 61
- [18] I. Valov, E. Linn, S. Tappertzhofen, S. Schmelzer, J. van den Hurk, F. Lentz, R. Waser, Nat. Comm. 4 (2013) (1) 1771
- [19] A.J. Bard, L.R. Faulkner, H.S. White, *Electrochemical methods: fundamentals and applications*, John Wiley & Sons (2022).
- [20] L. Matějová, V. Valeš, R. Fajgar, Z. Matěj, V. Holý, O. Šolcová, J. Sol. State Chem. 198 (2013) 485
- [21] V. Valeš, L. Matějová, Z. Matěj, T. Brunátová, V. Holý, J. Phys. and Chem. Solids 75 (2014) (2) 265
- [22] C. Ophus, *Microscopy and Microanalysis* **25** (2019) (3) 563
- [23] S. Kim, S.K. Kim, S. Khodorov, J. Maier, I. Lubomirsky, *Phys Chem Chem Phys* 18 (2016) (4) 3023
- [24] J. Koettgen, S. Grieshammer, P. Hein, B.O. Grope, M. Nakayama, M. Martin, *Phys Chem Chem Phys* 20 (2018) (21) 14291
- [25] J. Bisquert, G. Garcia-Belmonte, P. Bueno, E. Longo, L. Bulhoes, J. Electroanal. Chem. 452 (1998) (2) 229
- [26] D. Mullins, S. Overbury, D. Huntley, Surface Science 409 (1998) (2) 307
- [27] E. Bêche, P. Charvin, D. Perarnau, S. Abanades, G. Flamant, Surface and Interface Analysis: An International Journal devoted to the development and application of techniques for the analysis of surfaces, interfaces and thin films 40 (2008) (3-4) 264
- [28] T.T.B. Lan, Y.-T. Li, A.-C.A. Sun, H.-C. Lu, S.-F. Wang, *Materials Science in Semiconductor Processing* 137 (2022) 106177
- [29] S. Moon, K. Park, P.H. Chung, D.P. Sahu, T.-S. Yoon, J. Alloys Compd. 963 (2023) 171211
- [30] S.K. Kim, S. Khodorov, I. Lubomirsky, S. Kim, *Phys Chem Chem Phys* 16 (2014) (28) 14961
- [31] S. Kim, J. Maier, J. Elecrochem. Soc. 149 (2002) (10) J73
- [32] R. Schmitt, J. Spring, R. Korobko, J.L.M. Rupp, Acs Nano 11 (2017) (9) 8881
- [33] R. Schmitt, M. Kubicek, E. Sediva, M. Trassin, M.C. Weber, A. Rossi, H. Hutter, J. Kreisel, M. Fiebig, J.L.M. Rupp, *Adv. Func. Mater.* **29** (2019) (5)
- [34] F. Messerschmitt, M. Kubicek, S. Schweiger, J.L.M. Rupp, Adv. Func. Mater. 24 (2014) (47) 7448